



Scour depth prediction at the base of longitudinal walls: a combined experimental, numerical, and field study

A. Khosronejad¹ · P. Diplas² · D. Angelidis¹ · Z. Zhang¹ · N. Heydari² · F. Sotiropoulos¹

Received: 27 November 2018 / Accepted: 24 June 2019 / Published online: 2 July 2019
© Springer Nature B.V. 2019

Abstract

A series of small- and large-scale experiments and numerical simulations were carried out to produce datasets for maximum scour depth at the base of longitudinal structures. The small-scale experimental datasets were employed to develop an empirical relationship for predicting maximum *local* scour depth. The measured datasets for scour patterns and depths were used to validate the accuracy of our morphodynamics model, the Virtual Flow Simulator (VFS-Geophysics). The large-scale experimental measurements and numerical simulations lead to the development of another empirical relationship to estimate the maximum *general* scour depth near the longitudinal structures in large-scale meandering streams/rivers. The premise of this study is that the maximum scour depths obtained from the two equations can be used independently to represent local and general scour at the base of longitudinal walls in meandering rivers. However, for a more conservative prediction, the two can be linearly summed up to obtain a total maximum scour depth. The presented correlations illustrate regression goodness of $r^2=0.63$ and 0.82 for the maximum local and general scour depth equations, respectively. Nonetheless, the developed equations are valid within a specific range of parameter for the sediment material, flow field, and waterway characteristics.

Keywords Longitudinal wall · Sediment transport · Scour depth · Numerical modeling · Experimental modeling

1 Introduction

Longitudinal structures, such as retaining walls, are widely used to enhance the slope stability of earth material, to protect bridge abutments and other longitudinal structures that encroach into waterways [8, 29, 30]. In meandering rivers flowing through urban areas or along roadways, longitudinal walls are commonly used as a countermeasure to prevent streambank erosion [13]. Characteristic structures include vertical and/or sloping walls that are constructed of rocks, cable-tied blocks, geo-bags or steel sheet pile [28, 32]. When

✉ F. Sotiropoulos
fotis.sotiropoulos@stonybrook.edu

¹ Civil Engineering Department, Stony Brook University, Stony Brook, NY, USA

² Civil and Environmental Engineering Department, Lehigh University, Bethlehem, PA, USA

installed at a riverbank, however, the base of a longitudinal wall itself is subjected to erosion by turbulent flow, resulting in exposure of its foundation. Full or partial exposure of the foundation can result in the failure of the structure. Thus, longitudinal walls need to be designed in a way that they are protected against scour. Yet, a critical component missing from the proper design and installation of longitudinal walls is the ability to predict accurately the maximum depth of scour along the base of the longitudinal wall.

To date, the maximum scour depth along the base of longitudinal wall structures is estimated based on unreliable rule-of-thumb guidance. Among the limited number of studies (see, e.g., [1, 6, 9, 31]), the most commonly utilized relation to compute the local scour depth around vertical and sloping longitudinal walls is an analytical-empirical formula employed in [13] and [14]. This formula resulted from analytical simplifications to evaluate potential scour along a vertical wall [14]. It relates the maximum scour depth (H_s) to the mean-flow depth (H), Froude number (Fr), and the angle (α) between the impinging flow direction and the vertical wall, also known as approach angle or angle of attack, as follows:

$$\frac{H_s}{H} = (0.73 + 0.14\pi Fr^2)\cos\alpha + 4Fr^{1/3}\sin\alpha, \quad (1)$$

where α varies from 0° to 90° for flow parallel and perpendicular to the longitudinal wall, respectively. Maynard [33] presented an empirical method for determining scour depths on a typical bend with sand bed materials. Maynard's method of estimating scour depth is based on a regression analysis of 215 data points extracted from laboratory investigations and field observations with return period of 1–5 years [33]. Maximum scour depth at the base of a longitudinal wall as defined in Maynard's best-fit formula for scour depth estimation is a function of channel aspect ratio (W/H), radius of river curvature (R_c) to river width (W) as follows:

$$\frac{H + H_s}{H} = 1.8 - 0.051 \frac{R_c}{W} + 0.0084 \frac{W}{H} \quad (2)$$

It is important to mention that Eq. (2) does not take into account critical parameters such as the flow velocity and the size of sediment materials and its correlation coefficient is $r^2 = 0.49$. Additionally, Maynard [34] acknowledged the need for more elaborative and physics-based studies of the phenomenon that could provide more accurate descriptions and estimates of the scour compared to the purely empirical derivations [34]. We note that both Eqs. (1) and (2) are limited to clear-water scour conditions. For live-bed conditions, HEC-23 [14] suggests that the maximum scour depth caused by bedforms should be added to these calculated scour depths.

The lack of unified and reliable guidelines to estimate the scour depth along the base of longitudinal structures has led practitioners to utilize the contraction scour relation of abutment design to provide a rough estimation of maximum scour depth. Scour along the base of such longitudinal structures is the result of a combination of multiple processes including: (1) general scour that is the lowering of the bed elevation of channels due to the action of turbulent flow induced by the 3D topological characteristics; i.e., channel curvature (in planform) and its changes, or changes in channel width (contraction/expansion); and (2) local scour due to the presence of the high-energy turbulence and locally increased shear stress at the leading edge of the longitudinal wall. Scour depth prediction at the base of longitudinal walls becomes even more intricate considering the fact that maximum scour events often occur during peak flood stages when field observations are both difficult and

dangerous, and the resulting scour holes may be partially or completely filled during the recession of the passing floods [12]. This process results in maximum scour depths often going unobserved without a costly and potentially dangerous effort. Some of the typical engineering approaches used today, mainly by geotechnical experts, is to estimate the scour depth based on empirical guidance to ensure that maximum scour depths do not reach the base of the longitudinal structure to avoid failure. For instance, it is recommended that for walls constructed along rivers and streams where the depth of scour has been determined, a minimum embedment of 0.6 m below this depth should be considered as the foundation level [14].

Hence, it is evident that the development of reliable and comprehensive relationships to predict accurately the maximum scour depth at the base of longitudinal walls in rivers and waterways is essential. To this end, one needs to take into account all the effective parameters including turbulent flow dynamics, sediment transport, and waterway characteristics. It is also critical to understand the complex environments and dynamic interaction between the hydrodynamic and geomorphic systems near the longitudinal walls. Current guidelines, detailed in HEC-23 [14], are often considered excessively conservative; lacking many of the effective parameters including the soil characteristics, wall roughness and slope, flow discharge, and meander characteristics [6, 9, 31, 32]. An adequate relationship for maximum scour prediction must take into account both local and general scour processes.

Local scour can also result from the acceleration of the flow around the wall leading edge and along the base of the longitudinal structure, the roughness transition imposed by the presence of the wall, and the generation of large-scale energetic vortices shed from the wall. Additionally, longitudinal walls installed along both inner and outer banks throughout meandering rivers may also experience significant *general* scour and deposition along the meander wave length—due to effects of channel curvature and/or channel width variation as a results of longitudinal wall installation along the bends. The combination of the two scour processes, local and general, can significantly increase the risk of structure failure. During flooding events, the hydrodynamic processes accelerate these local and general scour mechanisms and endanger the structural integrity of longitudinal wall structures by reducing the passive resistance and overall bearing capacity of the foundations (Fig. 1). Abrupt changes in river-bank roughness and stepped transitions at the leading edge of the longitudinal structures can introduce complex large-scale energetic coherent structures in the surrounding flow environments. The vortices give rise to complex sediment transport phenomena and scouring dynamics originating at the exposed upstream edge of the structure. Thus, the effective roughness height of the longitudinal walls is a crucial parameter for accurate estimation of local and general scour at the base of these structures.

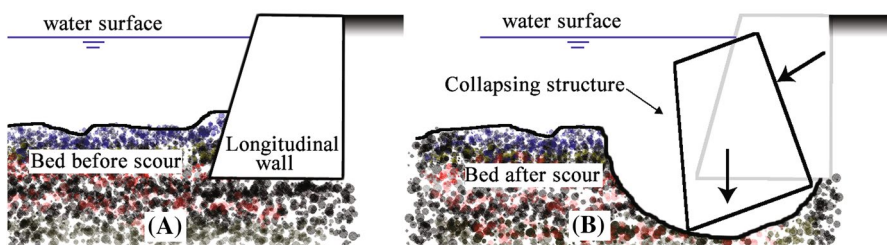


Fig. 1 Schematic of a longitudinal wall before (a) and after scour at the base (b), which can lead to the failure of the structure. Flow is perpendicular to the plane of the picture

In this study, we present measurements obtained from laboratory experiments and high-fidelity numerical simulations to develop regression equations for predicting maximum scour depth at the base of longitudinal walls. These equations consider most of the effective flow, sediment, and waterway parameters, including: sediment particle median grain size, mean-flow velocity, mean-flow depth, angle of installation, effective roughness of longitudinal walls, channel sinuosity and bank slope [38]. We develop two separate equations relevant to the maximum scour depth due to local and general scour processes. One equation is developed based on our indoor flume experimental data to represent the maximum scour depth at the leading edge of longitudinal walls due to local scour. The other equation is developed based on data obtained from (1) parametric numerical simulations using our in-house code, the Virtual Flow Simulator (VFS-Geophysics) and (2) experimental tests at the Outdoor StreamLab (OSL) of St. Anthony Falls Laboratory [22] to represent the maximum scour depth at the base of longitudinal walls due to general scour process. The numerical and experimental large-scale tests account for the effects of the river topological characteristics and the structure-induced channel contraction on the maximum scour depth along the base of the longitudinal walls. We hypothesize that a linear summation of the two maximum scour depths, using the equations proposed in this work, yields a overly conservative value for the total scour depth at the base of longitudinal walls. This is mainly because the two scours (general and local) take place at different locations along the length of longitudinal walls. Utilization of the proposed equations to estimate the scour depths associated with each of the two scour processes enables fast and low-cost assessment of maximum scour depth at different locations along these longitudinal structures, while making sure that the engineering standards remain at a high level. Our approach also contributes in minimization of the economic impact of design, installation, monitoring and maintenance of the structures.

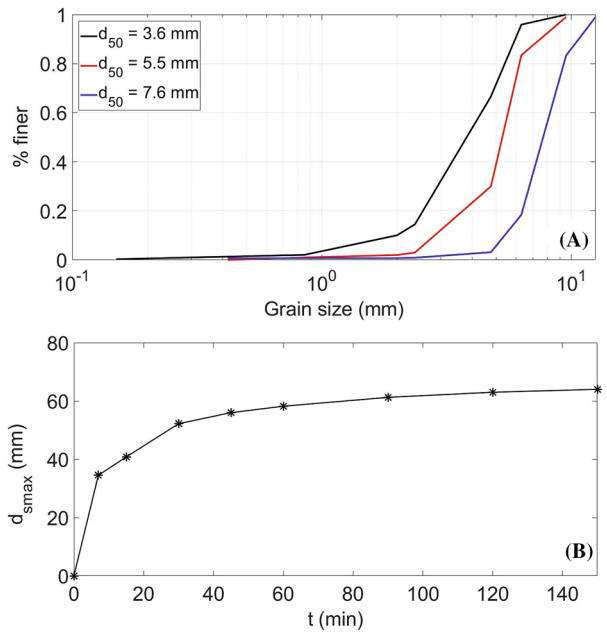
This paper is organized as follows. First, we present the small-scale experiments. Then, the large-scale experimental tests at the OSL will be presented and followed by the numerical simulations of large-scale test cases. Subsequently, we present the proposed equations for local and general scour depth prediction at the base of longitudinal walls. Finally, we summarized the findings of this work. “Appendices 1 and 2” describe the governing equations and validation of the numerical model, respectively.

2 Small-scale experiments

The small-scale experiments were conducted in a 15 m long, 1.2 m wide and 0.6 m deep recirculating tilting flume, located at the Imbt Hydraulic Laboratory of Lehigh University. The reference channel bed, used in most of the experiments, was covered with a 0.1 m thick layer of gravel with $d_{50} = 3.6$ mm and $d_{90} = 6.0$ mm. The geometric standard deviation ($\sigma_g = \sqrt{\frac{d_{84}}{d_{16}}}$) and the angle of repose of the bed material, measured via fixed funnel method, were 1.53 and 36° , respectively. To examine the effect of sediment size on the maximum scour depth at the equilibrium state, coarser bed material with d_{50} of 5.5 mm and 7.6 mm were utilized in some of the experiments. Figure 2a depicts the grain size distribution of the bed materials used in the present work. It should be noted that the bed material shape was predominantly sub-rounded with less than 5% platy particles.

A model retaining wall structure, made of Plexiglas, was installed 10.2 m downstream of the channel inlet. It was sufficiently long (1 m) to render the local scour/deposition processes independent of the structure dimension. Furthermore, the upstream channel section

Fig. 2 Grain size distribution of the bed materials used in the small-scale experiment (a). Temporal evolution of maximum scour depth at the base of the retaining wall during a preliminary experiment (b)



provided sufficient length to allow the approach flow to attain a fully developed condition before it reached the test area. This was verified by collecting several velocity profiles along the channel centerline using an acoustic Doppler velocimetry (ADV). Hollow glass spheres with a mean diameter of 10 μ m were used as seeding material to enhance the signal to noise ratio. The experiments were conducted in the presence of only one channel bank. It was installed on the right side of the flume where the retaining wall was mounted (Fig. 3). Bank angles of $\theta = 28^\circ, 35^\circ, 45^\circ,$ and 70° were considered in the present work. For $\theta = 28^\circ$ and 35° the bank material was identical to the reference channel bed. For the larger bank angles, however, wooden boards were employed. The local degree of contraction due to the presence of the retaining wall was kept $< 20\%$ to ensure that scour due to contraction is minimized [2, 5]. More specifically it ranged between 13.3 and 19.2% for $\theta = 28^\circ$; 11.4% and 15.6% $\theta = 35^\circ$; 8.7% and 12% for $\theta = 45^\circ$; and about 4% for $\theta = 70^\circ$.

The experimental flow conditions were designed following two main criteria: (1) clear-water scour condition and (2) subcritical flow with a Fr number at or below 0.5. The latter

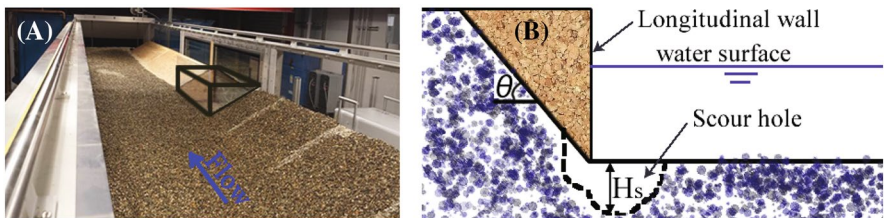


Fig. 3 The small-scale experimental flume (a) and a sketch of the sloped side-bank with longitudinal wall (b). The maximum local scour depth H_s is measured after each test. In b, flow is in the out-of-plane direction

criterion was intended to reproduce conditions that are typical of those encountered in the field. To satisfy the former criterion, the flow parameters for each experiment were selected to produce near threshold of motion conditions in the upstream section of the flume. This was mainly guided by the critical value of the Shields stress parameter ($\tau^* = \frac{HS}{Rd_{50}}$, where S is channel bed slope, and $R = (\rho_s - \rho)/\rho$ is submerged specific density), and visual inspection to ensure existence of very sporadic movement of particles upstream of the test section. For each experiment, first, the flume was gently filled with water to avoid a significant disturbance of the initial channel topography. Then, the tailgate was lowered and the flow rate was slowly increased to reach the desired value. The run time for each experiment was 2.5 h. The selection of this duration was guided by preliminary experiments, which exhibited minor changes in the depth and geometry of the scour hole for a period longer than 2.5 h. Figure 2b depicts the temporal evolution of maximum scour depth at the base of the retaining wall during a preliminary experiment. Previous studies also support the notion that local scour develops very rapidly and most of the erosion occurs during the initial stages of the experiment [4, 43]. Therefore, the run time adopted for the present experiments was deemed sufficiently long to represent equilibrium scour conditions. Upon completion of each experiment, the flume was slowly drained, and the maximum scour depth was measured using a point gauge with an accuracy of ± 0.01 mm.

Overall, 64 experimental tests were performed under varying flow conditions to record the maximum scour depth at the base of the longitudinal wall at the equilibrium condition. The range of various variables is reported in Table 1. Further details about the small-scale experiments can be found in [38].

3 Large-scale experiments

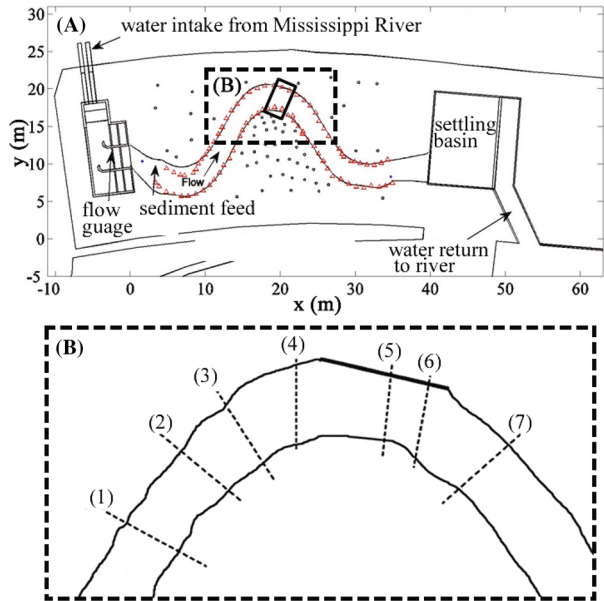
Large-scale experiments to quantify scour at the base of longitudinal structures were conducted in the OSL. The goal of these experiments was to examine the effect of wall angle, also known as approach angle, and wall roughness on scour at the base of a vertical longitudinal wall in a meandering channel. The OSL is a field-scale experimental facility with the ability to independently control flow and sediment feed (Fig. 4a). This arrangement facilitates examination of flow and sediment transport phenomena under well-controlled conditions with channel's geometrical characteristics resembling those typically encountered in the field. The experimental test section is located within the middle meander bend of the mobile-bed channel with a median grain size of 0.7 mm and a sinuosity of $\bar{s} = 1.3$. OSL is equipped with a high-resolution data acquisition (DAQ) carriage—specifically designed for it. The DAQ carriage enables the precise positioning of instrumentation in

Table 1 Range of variables in the small-scale experiments

Range	d_{50} (mm)	θ (°)	S (%)	H (m)	U_b (ms ⁻¹)	τ^*	H_s (m)
Minimum	3.6	35	0.02	0.13	0.36	0.01	0.015
Maximum	7.6	70	0.4	0.21	0.73	0.12	0.1

d_{50} is the median grain size of bed material, θ is the angle of sloped right-bank, S is the slope of channel bed, H is the mean-flow water depth, U_b is the mean-flow velocity, τ^* is the critical Shields stress parameter, and H_s is the maximum scour depth around the model of longitudinal wall in the flume

Fig. 4 Schematic of Outdoor StreamLab (OSL) from top view (a) and seven transects along which the bed-elevation profiles are measured (b). The topography cart was placed at the black rectangle and surveyed into the OSL coordinate system. Red triangles and black circles show the location of benchmark points of the OSL side banks and water quality stations, respectively



all three dimensions. An ultrasonic transducer was used to record water surface elevations, while the bed topography was measured using a subaqueous sonar. Both of the two instruments were installed on the DAQ carriage. Water discharge and sediment feed measurements were monitored at the inlet.

Prior to the installation of longitudinal walls, we ran a baseline experiment (starting from flatbed) to document the flow and bed topography of the OSL (without longitudinal wall). Subsequently, four experimental runs were conducted in the OSL to investigate (1) two different longitudinal wall roughness characteristics and (2) two different approach angles. Starting from flat sediment bed (see Fig. 10), all test cases and the baseline case were run under bankfull flow condition with volumetric flow rate, mean-flow depth, and bulk velocity of $0.28 \text{ m}^3/\text{s}$, $\sim 0.3 \text{ m}$, and $\sim 0.32 \text{ m/s}$, respectively, obtaining a Reynolds number of $Re = 95 \times 10^3$ and Froude number of $Fr = 0.19$. For each case, the cross-sectional topography of the OSL around the longitudinal walls was monitored approximately every hour with a point gauge mounted on the DAQ. Longitudinal walls were installed with two different approach angles of 30° and 40° in the same approximate location (Fig. 5). Each wall was installed at least 0.2 m below the depth of maximum scour prior to wall installation and was carefully checked to ensure it was vertical. The wall location was surveyed to verify as built dimensions. Experimental runs included rough and smooth walls. The smooth wall (Fig. 5b) was constructed of a smooth plastic plate and the rough wall (Fig. 5a) was created by gluing pea gravel material (with effective roughness height of $\sim 0.01 \text{ m}$) on the plastic plate. The four test cases 1–4 are defined as smooth wall with angle of attack of 30° , rough wall with angle of attack of 40° , smooth wall with angle of attack of 40° , and rough wall with angle of attack of 40° , respectively.

In each test case, the bed topography of the OSL was hourly monitored along seven transects (Fig. 4b). Once at dynamic equilibrium (after about 8 h), the maximum scour depth and bed profiles along the seven transect were measured. We present in Table 2 the maximum scour depth of each test cases. Figure 6 plots the measured location of the maximum

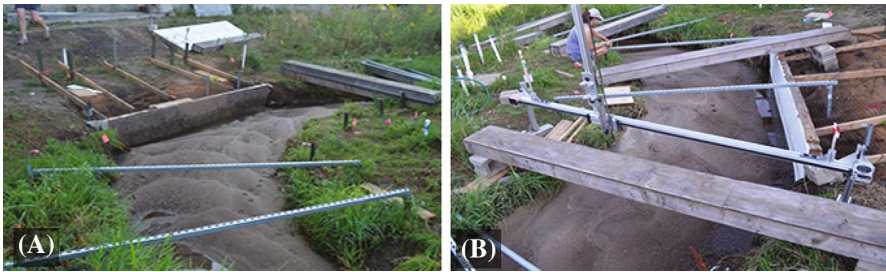


Fig. 5 Rough (a) and smooth (b) longitudinal walls installed in the OSL immediately downstream of the meander apex

Table 2 Maximum scour depth (H_s) measured in the OSL at the base of the longitudinal walls in test cases 1–4 and the baseline case

Test case	H_s (m)
Baseline	0.11
1	0.22
2	0.22
3	0.18
4	0.18

H_s is measured as the difference between the flatbed elevation and the scoured elevation

scour depth along the longitudinal walls in each test case, while details of the measured data can be found in [38]. The data collected from the OSL were used to (1) develop the general scour equation and (2) validate the VFS-Geophysics model (see “Appendix 2”). Taken alone, the OSL data imply that wall roughness has small to no effect on maximum scour depth and its location—likely due to the roughness of the channel and vegetated banks (see Fig. 6 and Table 2). Wall angle relative to the approach flow also has relatively small effect on the scour depth. While, wall angles has also influenced the location of maximum scour depth: the larger angle resulted in scour shifted downstream and away from the wall. The four test cases of the large-scale experiments obtained four data points, which are used (along with the numerical simulation results) in Sect. 5 to derive general scour equation. Details of the physical modeling in this section can be found in [38].

4 Numerical simulations

We employed the VFS-Geophysics model to produce data points for maximum scour depth around longitudinal walls in two virtual sand- and gravel-bed meandering rivers. The two virtual rivers were obtained based on a comprehensive analysis of the previously published data, as described in [23], to represent natural meandering rivers. The sand-bed river type corresponds to rivers with small longitudinal bed slope and great sinuosity, while the gravel-bed rivers includes mountainous rivers and streams with high bed slope and small sinuosity. The selected parameter values for the sand- and gravel-bed river test-beds are summarized in Table 3. For more details regarding the numerical simulations the reader is also referred to [21, 38]. For the sake of brevity, herein we only

Fig. 6 Locations of the maximum scour depth (orange circles) along the base of the longitudinal walls (dashed red lines) in the OSL for test case 1 (a), 2 (b), 3 (c), and 4 (d). Arrows represent the measured velocity vectors (using an ADV) at the mid-depth of the flow along four different transects measured. Black lines represent the side banks of the OSL. Color maps show the contours of bed elevation [z (m)] (above sea level) scanned using the high-resolution scanned of the topography cart at quasi-equilibrium in small windows adjacent to the walls (see the location of topography cart in Fig. 4a). Flow is from left to right

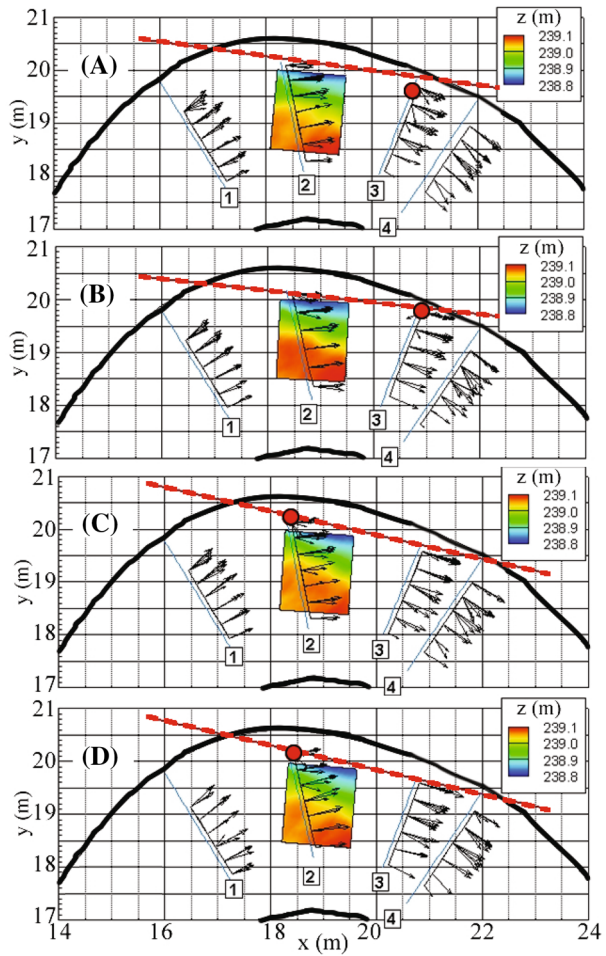


Table 3 Characteristics of selected channels based on the hydraulic geometry relationships for sand and gravel rivers with bankfull flow conditions, including median grain size of bed material [d_{50} (cm)], density of sediment material [ρ_s (kg/m^3)], channel width [B (m)], flow discharge [Q (m^3/s)], flow depth [H (m)], bed slope (S), sinuosity (\bar{s}), and wave length of meander [λ (m)]

River type	d_{50}	ρ_s	B	Q	H	S	\bar{s}	λ
Gravel-bed	3.2	2650	27	36	0.9	3.2×10^{-3}	1.15	328.1
Sand-bed	0.5	2650	27	48.4	1.35	7.0×10^{-4}	1.5	266.7

present the analysis of the obtained dataset. It should be noted that prior to numerical simulations, we utilized the results of small- and large-scale experiments (mentioned above) to validate the numerical model, as reported in [21]. The validation study for a test case in the OSL is also presented in “Appendix 2”, while the governing equations and computational details of the model can be found in “Appendix 1”.

5 Experimental and numerical results

5.1 Small-scale tests: local scour depth prediction

The results obtained from small-scale indoor experiments (64 data points in Sect. 2) are used to develop an empirical relationship for estimating the maximum scour depth at the base of longitudinal walls. The experimental observations indicate that the maximum channel bed erosion in all cases occurs at the leading edge of the protrusion (Fig. 3). This is admittedly due to the abrupt transition from the channel bank to the vertical face of the longitudinal wall, which can significantly elevate local bed shear stresses and enhance bed material erosion [10, 35, 37]. Following dimensional analysis, the maximum local scour depth can be written as a function of independent dimensional variables. One possible set of such variables includes:

$$H_s = f(H, d_{50}, U_b, \theta, g, \nu, \rho, \rho_s) \quad (3)$$

where g is the gravitational acceleration, ν is the kinematic viscosity of water, ρ is the density of water, and ρ_s is the density of sediment material. Selecting ρ , d_{50} and g as the repeating variables, and following standard dimensional analysis procedures, Eq. (3) can be recast in terms of dimensionless parameters as follows:

$$\frac{H_s}{d_{50}} = f\left\langle \frac{H}{d_{50}}, Fr_d, \theta, Re_p, R \right\rangle \quad (4)$$

where $Re_p = U_b d_{50} / \nu$ is particle Reynolds number, $Fr_d = U_b / \sqrt{g d_{50}}$ is the grain-size Froude number, and $R = (\rho_s - \rho) / \rho$ is the submerged specific gravity of sediment material. Re_p is not as important for a fully rough boundary, where the friction factor (and critical Shields stress) becomes independent of particle Reynolds number. Additionally, for natural rivers, R is approximately constant. Therefore, Eq. (4) can be reduced to:

$$\frac{H_s}{d_{50}} = f\left\langle \frac{H}{d_{50}}, Fr_d, \theta \right\rangle \quad (5)$$

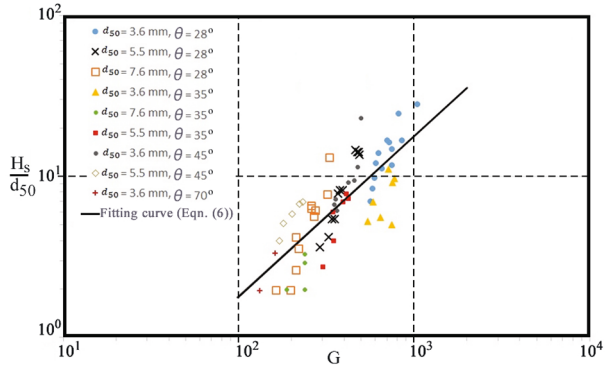
It should be emphasized that the above analysis is limited to non-cohesive sediment material. Using all 64 data points obtained from the experiments, and employing forward multiple regression analysis, the following expression is obtained:

$$\frac{H_s}{d_{50}} = 0.0178 \left\langle \frac{H}{d_{50}} \right\rangle^{1.24} \cot^{1.325}(\theta) Fr_d^{1.108} \quad (6)$$

Equation (6) has a goodness of fit of $r^2 = 0.63$ and covers a considerable range of bank slopes ($28^\circ \leq \theta \leq 70^\circ$), bed slopes ($0.09\% \leq S \leq 0.6\%$), relative roughness values ($17.9 \leq \frac{H}{d_{50}} \leq 62.5$), and grain-size Froude number ($1.59 \leq Fr_d \leq 3.89$). Figure 7 depicts the best-fit curve of the measured values of the maximum local scour depth and the combination of the independent variables. All variables in the proposed equation (Eq. 6) are statistically significant—with a p value of the exponents being less than 0.5%.

Equation (6) implies that the steeper the bank slope, the shallower the maximum local scour depth would be. More specifically, the measurements indicate that the maximum scour depth for 35° bank angle was 54% less than that recorded for 28° under the

Fig. 7 Regression of the small-scale experimental data to estimate the maximum local scour depth at the leading edge of the longitudinal structure. r^2 of the regression is 0.63. Abscissa represents $G = (H/d_{50})^{1.24} \cot^{1.325}(\theta) Fr_d^{1.108}$



baseline flow conditions, $S = 0.25\%$, $Q = 0.08 \text{ m}^3/\text{s}$, and $H = 0.17 \text{ m}$. For a bank angle larger than 70° , no local bed scour was detected.

Additionally, a set of experiments were conducted to investigate the effect of several other parameters, not included in Eq. (6), on the scour depth, namely, wall surface roughness, vegetation cover on the channel bank just upstream of the wall, and the presence of armor layer. The results indicate that wall roughness with an equivalent sand grain size of 0.6 mm reduced the maximum scour depth at the equilibrium condition by 30% . Coarser roughness elements, with a grain size of 3.6 mm , led to even a shallower scour depth, 57% less than that recorded for the smooth wall condition. This is mainly attributed to the increase in flow resistance and reduction of the flow velocity in the vicinity of the wall. This, in turn, can moderate the forces responsible for local scour development [3, 27]. Similar results were reported in [15]. They indicated that roughness elements on the outer vertical wall along a channel bend could reduce the maximum scour depth by up to 40% . The experimental observations also demonstrate that a dense vegetation cover on the channel bank immediately upstream of longitudinal walls can provide an effective means for reducing erosion. Specifically, in the present work, no scour was observed at the leading edge of the protrusion under the baseline hydraulic conditions with a dense vegetation cover on the bank. This constitutes a major improvement compared to the scour depth of 5.3 cm , recorded under the same conditions in the absence of any vegetation. Through a simple flow visualization technique it became apparent that the vegetation shifted the flow away from the channel bank in a very gradual manner, producing a more streamlined transition and thus minimizing the impact of the abrupt change in channel geometry and scour development at the leading edge of the retaining wall. Finally, the experimental observations reveal that as long as the armor layer material is dismantled due to a high flow velocity, it can no longer protect the subsurface material and limit the development of scour hole in the vicinity of longitudinal walls.

5.2 Large-scale tests: general scour depth prediction

The results from OSL experiments (four data points in Sect. 3) are combined with the numerical simulations results (20 data points in Sect. 4) to develop an empirical relationship for estimating the maximum scour depth at the base of longitudinal walls due to general scour [38]. It is found that for most cases the maximum scour depth due to general scour occurs near the mid-length of the longitudinal walls. Similar to the analysis for the local scour data in Sect. 2,

Fig. 8 Schematic of a meander bend showing the installation angles (ψ) of the longitudinal wall, wavelength (λ_m), arc-length (λ) and amplitude (A_m) of the meander

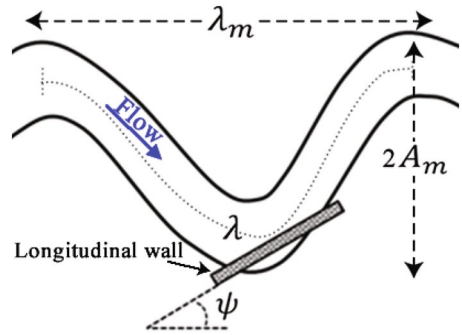
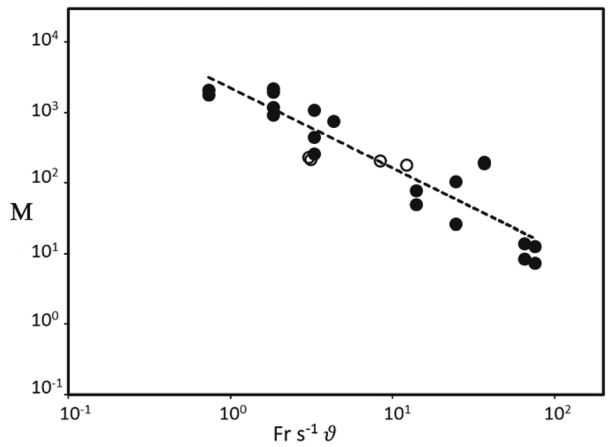


Fig. 9 Maximum scour depth data obtained from large-scale experiments (hollow circles) and numerical simulations (bold circles) for general scour. Dashed line represents the regression equation overlapping the data points. r^2 of the regression is 0.821. Ordinate represents $M = H_s/d_{50} - \frac{8}{5}Fr_d - \frac{3\pi}{2}e^{(k_s/H)^{1/10}}$



via dimensional analysis, parameters influencing the maximum scour depth due to general scour along the length of the walls are as follows:

$$H_s = f(d_{50}, U_b, H, S, \lambda_m, A_m, g, k_s, \psi) \tag{7}$$

where S is the bed slope of the channel, λ_m is the wavelength of the meander bend, A_m is the amplitude of the meander bend, k_s is the effective roughness height of the surface of the longitudinal wall, and ψ is the angle that longitudinal wall makes with the tangent to the river bank at its apex (Fig. 8). Therefore, ψ for a straight channel is zero.

The maximum scour depth due to general scour can be best found if scaled with d_{50} , which varies between 0.1 to 32 mm for our large-scale tests (for more details of the selected representative ranges of parameters see [18, 21, 23]). The characteristics of meander bend can also be best expressed via its sinuosity ($\tilde{s} = \lambda_m/\lambda$). Therefore, Eq. (7) in its non-dimensional form can be rewritten as:

$$\frac{H_s}{d_{50}} = f\left\langle Fr, Fr_d, \tan\psi, \tilde{s}, \frac{k_s}{H} \right\rangle \tag{8}$$

We analyzed numerous methods to best represent the bulk of these data in an empirical relationship (Fig. 9) and found that the following equation provides the best overlap:

Table 4 Range of variables in the large-scale experiments and numerical modelings

Range	d_{50}	W	Q	H	S	\bar{s}	λ_m	Fr	Fr_p	ψ	k_s/H
Minimum	0.7	2.5	0.3	0.2	0.07	1.0	4.5	0.19	2.64	–20	0.03
Maximum	32	27	48.4	1.35	0.32	1.5	328.1	0.50	5.96	60	0.11

d_{50} (mm) is the median gran size of bed material, W (m) is the river width, Q (m³/s) is the volumetric flow rate, H (m) is the mean-flow depth, S (%) is the bed slope of the river, \bar{s} is the sinuosity of the river, λ_m (m) is the wave lengthen of the meander, Fr is the Froude number of the river flow, Fr_p is the grain-size Froude number, ψ (°) is the installation angle of the longitudinal wall, and k_s/H is the dimensionless effective roughness height of the longitudinal wall surface

$$\frac{H_s}{d_{50}} = 1909(Fr\bar{s}\vartheta)^{-10/9} + \frac{8}{5}Fr_d - \frac{3\pi}{2}e^{(k_s/H)^{1/10}} \tag{9}$$

where ϑ for gravel-bed rivers is expressed as:

$$\vartheta = \max\left\langle 150, \frac{1}{\tan^2\psi} \right\rangle, \tag{10}$$

and, for the sand-bed rivers it is found to be:

$$\vartheta = \max\left\langle 100, \frac{1}{\tan^2\psi} \right\rangle, \tag{11}$$

Equation (9) has a correlation coefficient of $r^2 = 0.821$ and the following limitations:

1. It is only applicable for rivers and streams with non-cohesive material;
2. It is developed for rivers under bankfull flow conditions and, thus, use of this equation for base-flow condition can result in misleading predictions;
3. It is best applicable for rivers that have geometry, flow, and sediment characteristics within the range of the large-scale rivers studied in this work (Table 4);
4. Scour hole due to the intrusion of the upstream edge of the longitudinal wall is not considered in obtaining the dataset for this equation and such scour depth needs to be determined based on the small-scale laboratory experiments (Eq. 6).

Hence, we propose the use of Eq. (9) as a formula to calculate the maximum scour depth at the base of longitudinal walls in meandering rivers due to general scour process. To avoid misleading predictions, it is important, however, that the four above mentioned limitations to be considered.

6 Conclusion

The current state-of-the-art scour depth prediction near longitudinal walls is limited to two empirical equations, which are obtained from a limited number of experimental and field data. These existing methods of prediction do not take into account some important properties of flow, sediment and waterway geometry, including, for instance: median grain size of sediment material, mean-flow depth and velocity, and sinuosity of meandering rivers.

We herein attempt to fill the gap and develop a more comprehensive relationship for estimating the total scour depth at the base of longitudinal walls. To this end, we carried out a series of experimental and numerical investigations encompassing most of the important characteristics of the sediment, flow and waterway geometry. The present studies considered the effect of turbulence, sediment material, roughness of the structures, and river geometry on the scour depth at the base of longitudinal walls.

Initially, a series of small-scale laboratory experiments were conducted to produce adequate dataset for the local scour depth occurring at the leading edge of longitudinal walls. Based on these data points, we obtained a relationship for estimating the maximum scour depth in the vicinity of longitudinal walls due to local scour process (Eq. 6). A series of large-scale experiments were carried out to produce large-scale physical data for the validations of numerical model. The large-scale experiment data were also combined with numerous data points obtained from numerical simulations to develop a relationship for estimating the maximum scour depth at the base of longitudinal walls due to general scour (Eq. 9). Since the maximum scour depth due to local and the general scour processes occur at different locations along the longitudinal walls; these estimated values can be considered separately to describe the scour depth at the leading edge and mid-length of the longitudinal walls, respectively. However, a linear combination of local and general scours can be also used to obtain a conservative value for the total maximum scour depth at the base of longitudinal walls in streams and rivers.

Acknowledgements This work was supported by National Cooperative Highway Research Program Grants NCHRP-HR 24–33 and 24–36.

Appendix 1: Governing equations of the numerical model

The detailed description of VFS-Geophysics mathematical formulations, hydro-morphodynamic coupling method, and boundary conditions can be found in [24]—see also [16, 17, 19, 22]. Herein, we briefly outline the equations that govern the hydrodynamics and morphodynamics of the model.

Hydrodynamic model

The hydrodynamic model solves numerically the unsteady, three-dimensional, incompressible Reynolds-averaged Navier–Stokes and continuity equations. The governing equations in generalized curvilinear coordinates, read as follows [20]:

$$J \frac{\partial U^j}{\partial \xi^j} = 0 \quad (12)$$

$$\frac{1}{J} \frac{\partial U^i}{\partial t} + \frac{\xi^i}{\xi^{x_o}} \left(\frac{\partial}{\partial \xi^j} (U^j u_o) + \frac{\partial}{\partial \xi^j} \left(\frac{\xi^j}{\xi^{x_o}} p \right) - \frac{1}{Re} \frac{\partial}{\partial \xi^j} \left(\frac{g^{jk}}{J} \frac{\partial u_o}{\partial \xi^k} \right) + \frac{\partial \tau_{oj}}{\partial \xi^j} \right) = 0 \quad (13)$$

where $\{x_i\}$ and $\{\xi^i\}$ are the Cartesian and generalized coordinates ($i=1,2, \text{ and } 3$), respectively, J is the Jacobian of the geometric transformation $J = \partial(\xi^1 \xi^2, \xi^3) / \partial(x_1, x_2, x_3)$, $\xi^i_{x_o} = \partial \xi^i / \partial x_o$ are the metrics of the geometric transformation, $\{u_o\}$ are the Cartesian veloc-

ity components, $U^i = \xi_{x_m}^i u_m / J$ are the contravariant components of the volume flux vector, $g^{jk} = \xi_{x_o}^j \xi_{x_o}^k$ are the components of the contravariant metric tensor, p is the pressure, τ_{ij} is the Reynolds stress tensor, Re is the Reynolds number ($= \frac{hU_m}{\nu}$), h is the mean-flow depth, U_m is the mean flow velocity, and ν is the kinematic viscosity of water. The above equations are closed using the $k - \omega$ model [40] to calculate the eddy viscosity. The turbulence closure equations in generalized curvilinear coordinates can be found in [24].

The governing equations are discretized in space on a hybrid staggered/non-staggered grid arrangement [11] using the second-order accurate QUICK scheme for the convective terms along with second-order accurate, three-point central differencing for the divergence, pressure gradient and viscous-like terms. The time derivatives are discretized using second-order backward differencing [16]. The discrete mean flow equations are integrated in time using an efficient, second-order accurate fractional step methodology coupled with a Jacobian-free, Newton–Krylov solver for the momentum equations and a GMRES solver enhanced with multigrid as preconditioner for the Poisson equation.

Morphodynamic model

The temporal variation of the river bed elevation is governed by the Exner-Polya equation [36]:

$$(1 - \gamma) \frac{\partial z_b}{\partial t} + \nabla \cdot \mathbf{q}_{BL} = D_b - E_b \tag{14}$$

where γ is the sediment material porosity, z_b is the bed elevation, ∇ denotes the divergence operator, \mathbf{q}_{BL} is the bed-load flux vector, D_b is the net deposition onto the bed, and E_b is the net entrainment from the bed cell. The motion of sediment in suspended load is governed by the following convection–diffusion equation [41, 42]:

$$\frac{1}{J} \frac{\partial(\rho\psi)}{\partial t} + \frac{\partial}{\partial \xi^j} (\rho\psi (U^j - W^j \delta_{i3})) = \frac{\partial}{\partial \xi^j} \left((\sigma_L^* \mu + \sigma_T^* \mu_i) \frac{G^{jk}}{J} \frac{\partial \psi}{\partial \xi^k} \right) \tag{15}$$

where $W^j = \left(\xi_3^j / J \right) w_s$ is the contravariant volume flux of suspended sediment, σ_L^* and σ_R^* are the laminar ($= 1/200$) and turbulent ($= 4/3$) Schmidt numbers, ρ is the density of water, and w_s is the settling velocity of non-spherical sediment particles which is computed by van Rijn’s formula [39].

At the mobile sediment/water interface we employ the approach proposed by Chou and Fringer [7] to specify boundary conditions for ψ using van Rijn’s pickup function [39]. At rigid walls and the outlet of the flow domain we employ a Neumann, zero-gradient boundary condition while for the free-surface boundary we assume free-slip condition [39]. For details regarding the equations and their boundary condition we employ to model the various terms in the above equations see [22, 24].

Appendix 2: Model validation

The VFS-Geophysics model is extensively validated for morphodynamics computations against laboratory- and field-scale data [22–24]. Herein, we present the results of yet another validation study using the sediment transport data obtained in the OSL for the test

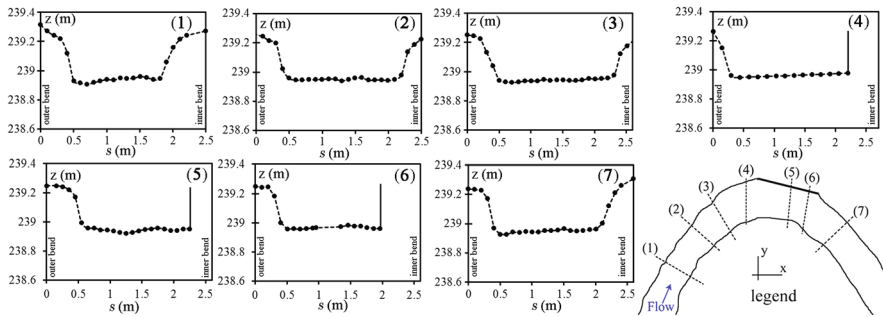


Fig. 10 Initial bed elevations profiles at the beginning of the simulations and experiments (black dotted lines). The location of cross-sections is shown in legend

case 3, which includes an installed longitudinal wall (smooth) an angle of attach of 40° . Validation studies for other test cases can be found in [23, 38]. As in the experiment, the numerical simulations started from flat sediment bed (see Fig. 10) and continued until the bed morphology reached a dynamic equilibrium. Once at the quasi-equilibrium, a subaqueous bed scanner was used to measure the bed topography of the OSL. These bed measurements represent instantaneous bed elevation of the OSL after $t \sim 8$ h during which OSL was at dynamic quasi-equilibrium, which can be characterized by the migration of mature bedforms. The amplitude of the experimentally observed bedforms was about 0.1–0.2 m while their wavelength varies between 0.5 and 1.0 m.

The initial bed topography of the OSL was scanned and used to create the computational grid system, which consists of ~ 9.9 million grids with $1201 \times 201 \times 41$ nodes in streamwise, spanwise, and vertical directions, respectively. Given the vertical (~ 0.3 m), spanwise (~ 2.5 m), and longitudinal (~ 15 m) dimensions of the OSL, the spatial resolution of the grid, which is uniformly distributed, is about ~ 0.01 m. The initial bed profiles in the experiment and, consequently, the model are shown in Fig. 10, while in Fig. 11a we plot the details of the computational grid system. Turbulence is modeled using large-eddy simulation (LES) module of the VFS-Geophysics model [25, 26]. A time step of 0.1 s was utilized for the flow field calculations to ensure a CFL number of less than 1.0. At the water surface, we prescribed the measured water-surface elevation as a sloping-lid boundary condition. A uniform flow is prescribe at the inlet of the OSL, while wall-modeling approach is used at the bed and side-walls of the OSL. The inlet boundary condition for the sediment transport model was prescribed with an inlet flux of 2 kg/min, which is consistent with the sediment feeding rate in the experiment.

We started the simulation by running the flow solver in the OSL under bankfull flow conditions. Once the flow field was statistically converged (which was established by motoring the kinetic energy within the computational domain), the morphodynamics module was activated. The coupled flow and morphodynamics simulation was continued until the bed morphology of the channel reached its quasi-equilibrium. The computed instantaneous vorticity field of the OSL is shown in Fig. 11c. The simulated time-averaged bed elevation and the root-mean-square (*rms*) of bed elevation fluctuations are shown in Fig. 11b, d, respectively. The simulated bedforms migrate and, thus, the bed bathymetry continuously evolves. The time-averaged bed elevations are computed to produce a bed bathymetry that can be better compared with the measured bed profiles.

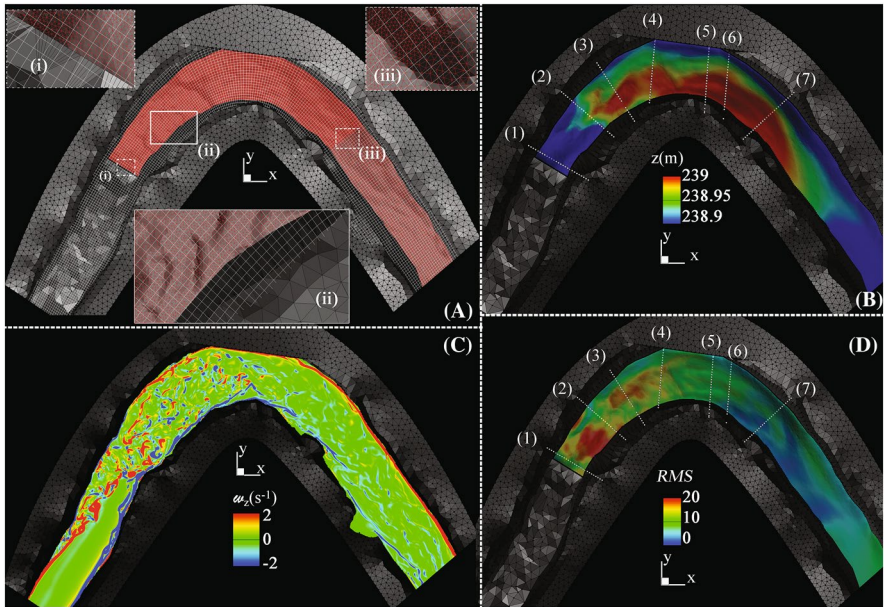


Fig. 11 Computational mesh (a) and simulated morphodynamics (b, d) and hydrodynamics (c) of the flow and sediment transport in the OSL with a longitudinal wall at the outer bend of the meander. The angle of attack of main flow to the wall is 40°. a Shows the computational mesh used to simulate OSL with an installed wall. Sediment transport equation is solved on the unstructured red triangular mesh, the white structured mesh is the background mesh on which the flow field is solved. The white square background mesh is skipped by a factor of 5 for the sake of visual clarity. The black-dots are the points surveyed in the OSL to produce the geometrical data. The grid resolution is almost uniform in all directions with a spacing of about 1.5 cm. b Shows the contours of time-averaged bed elevation; c depicts the computed contours of instantaneous out-of-plane vorticity at the water surface; and d is the computed *rms* (percent) of bed elevation fluctuations. Flow is from left to right

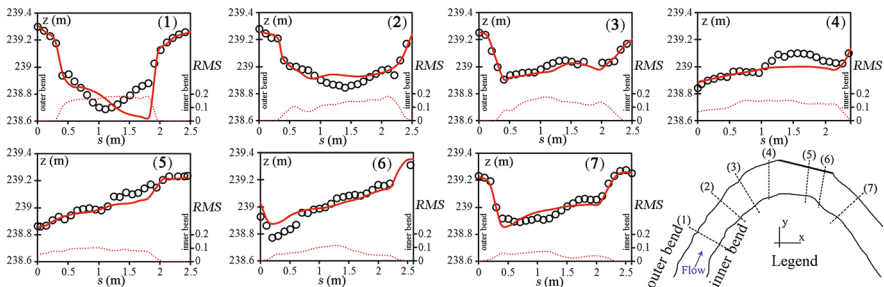


Fig. 12 Computed time-averaged (red lines) and measured instantaneous (black circles) bed elevation (z) profiles along six cross-sections of test case 3 (shown in legend). The vertical axis on the right represents *rms* of bed fluctuations (red dotted-line) for the simulated bed morphology and S (in m) is the vector along each cross-section. Note that since the river banks are almost stationary, the *rms* of fluctuation near the river banks approaches zero. While in the mid-channel, where migrating bedforms are present in the simulations, *rms* values vary between 0.1 with a maximum of ~ 0.2

In Fig. 12 we compare the simulated and measured bed profiles along the seven cross-sections shown in Fig. 11b. One can clearly see a major discrepancy between measured and simulated bed profiles for the first two cross-sections. The reason for such discrepancies can be attributed to the uncertainty in the inlet boundary condition. We note that the measured bed profiles in Fig. 12 are instantaneous while the simulated results are time-averaged. Overall, the agreement observed in Fig. 12 for the cross-sections three to seven is reasonably good and the mean error percentage is about 10%. Additionally, as one can see in this figure, the generic scour and deposition areas are well predicted. Finally, we note that the computed *rms* of the bed fluctuation in Fig. 12 is a good representative of the amplitude of the numerically captured bedforms. The computed *rms* of bed fluctuation within the channel varies between 0.08 and 0.18 m with a maximum of about 0.19 m, which seems consistent with the amplitude of the experimentally observed bedforms in the OSL.

References

1. Anderson S, Williams J (2002) Road stabilization, reconstruction, and maintenance with a combined mechanically stabilized earth and secant pile wall: Zion national park, utah. *J Transp Res Board* 1808(1):76–83
2. Ballio F, Teruzzi A, Radice A (2009) Constriction effects in clear-water scour at abutments. *J Hydraul Eng* 135:140–145. [https://doi.org/10.1061/\(ASCE\)0733-9429\(2009\)135:2\(140\)](https://doi.org/10.1061/(ASCE)0733-9429(2009)135:2(140))
3. Blanckaert K, Duarte A, Schleiss AJ (2010) Influence of shallowness, bank inclination and bank roughness on the variability of flow patterns and boundary shear stress due to secondary currents in straight open-channels. *Adv Water Resour* 33:1062–1074. <https://doi.org/10.1016/j.advwatres.2010.06.012>
4. Bouratsis P, Diplas P, Dances C, Apsilidis N (2017) Quantitative spatio-temporal characterization of scour at the base of a cylinder. *Water* 9:227. <https://doi.org/10.3390/w9030227>
5. Breusers H, Raudkivi A (1991) Scouring: hydraulic structures design manual series. CRC Press, Boca Raton
6. Carriaga C (2000) Scour evaluation program for toe-down depth assessment. In: Building partnerships, pp 1–10
7. Chou YJ, Fringer OB (2008) Modeling dilute sediment suspension using large-eddy simulation with a dynamic mixed model. *Phys Fluids* 20:115103
8. Collas F, Buijse A, van den Heuvel L, van Kessel N, Schoor M, Eerden H, Leuven R (2017) Longitudinal training dams mitigate effects of shipping on environmental conditions and fish density in the littoral zones of the river Rhine. *Sci Total Environ* 1183:619–620. <https://doi.org/10.1016/j.scitoenv.2017.10.299>
9. Davies R, Carriaga CC (2001) Scour evaluation procedure for determining toe-down depths of hydraulic structures. In: Bridging the gap, pp 1–9
10. Dey S, Barbhuiya A (2006) Flow field at a vertical-wall abutment. *J Hydraul Eng* 131:1126–1135. [https://doi.org/10.1061/\(ASCE\)0733-9429\(2005\)131:12\(1126\)](https://doi.org/10.1061/(ASCE)0733-9429(2005)131:12(1126))
11. Ge L, Sotiropoulos F (2007) A numerical method for solving the 3D unsteady incompressible navier-stokes equations in curvilinear domains with complex immersed boundaries. *J Comput Phys* 225:1782–1809
12. HEC-18 (2001) Evaluating scour at bridges: hydraulic engineering circular No. 18. U.S. Dept. of Transportation, Washington D.C.
13. HEC-20 (2001) Stream stability at highway structures: hydraulic engineering circular No. 20. U.S. Dept. of Transportation, Washington D.C.
14. HEC-23 (2001) Bridge scour and stream instability countermeasures: hydraulic engineering circular No. 23. U.S. Dept. of Transportation, Washington D.C.
15. Hersberger DS, Franca MJ, Schleiss AJ (2015) Wall-roughness effects on flow and scouring in curved channels with gravel beds. *J Hydraul Eng*. [https://doi.org/10.1061/\(asce\)hy.1943-7900.0001039](https://doi.org/10.1061/(asce)hy.1943-7900.0001039)

16. Kang S, Lightbody A, Hill C, Sotiropoulos F (2011) High-resolution numerical simulation of turbulence in natural waterways. *Adv Water Resour* 34(1):98–113
17. Kang S, Sotiropoulos F (2011) Flow phenomena and mechanisms in a field-scale experimental meandering channel with a pool-riffle sequence: insights gained via numerical simulation. *J Geophys Res* 116:F0301
18. Khosronejad A, Diplas P, Sotiropoulos F (2016) Simulation-based approach for in-stream structures design: Bendway weirs. *J Environ Fluid Mech*. <https://doi.org/10.1007/s10652-016-9452-5>
19. Khosronejad A, Kang S, Borazjani I, Sotiropoulos F (2011) Curvilinear immersed boundary method for simulating coupled flow and bed morphodynamic interactions due to sediment transport phenomena. *Adv Water Resour* 34(7):829–843
20. Khosronejad A, Kang S, Sotiropoulos F (2012) Experimental and computational investigation of local scour around bridge piers. *Adv Water Resour* 37:73–85
21. Khosronejad A, Kozarek J, Diplas P, Sotiropoulos F (2015) Simulation-based approach for in-stream structure design: J-hook vane structures. *J Hydraul Res* 53:588–608. <https://doi.org/10.1080/00221686.2015.1093037>
22. Khosronejad A, Kozarek J, Palmsted M, Sotiropoulos F (2015) Numerical simulation of large dunes in meandering streams and rivers with in-stream rock structures. *Adv Water Resour* 81:45–61
23. Khosronejad A, Kozarek JL, Diplas P, Hill C, Jha R, Chatanantavet P, Heydari N, Sotiropoulos F (2018) Simulation-based optimization of in-stream structures design: rock vanes. *Environ Fluid Mech* 18(3):695–738. <https://doi.org/10.1007/s10652-018-9579-7>
24. Khosronejad A, Kozarek JL, Sotiropoulos F (2014) Simulation-based approach for stream restoration structure design: model development and validation. *J Hydraul Eng* 140(7):1–16
25. Khosronejad A, Sotiropoulos F (2014) Numerical simulation of sand waves in a turbulent open channel flow. *J Fluid Mech* 753:150–216
26. Khosronejad A, Sotiropoulos F (2017) On the genesis and evolution of barchan dunes: morphodynamics. *J Fluid Mech* 815:117–148
27. Koochak P, Bajestan MS (2016) The effect of relative surface roughness on scour dimensions at the edge of horizontal apron. *Int J Sediment Res* 31:159–163. <https://doi.org/10.1016/j.ijsrc.2013.02.001>
28. Lagasse PF, Spitz WJ, Zevenbergen LW, Zachman DW (2004) Handbook for predicting stream meander migration using aerial photographs and maps. National Cooperative Highway Research Council, NCHRP 533, National Research Council
29. Le B (2018) Training rivers with longitudinal walls: long-term morphological responses. Master's thesis, Delft University of Technology. <https://doi.org/10.4233/uuid:cf588b41-0bcc-490f-9cf0-ea0d95a92678>
30. Le T, Crosato A, Mosselman E, Uijttewaal W (2018) On the stability of river bifurcations created by longitudinal training walls. Numerical investigation. *Adv Water Resour*. <https://doi.org/10.1016/j.advwatres.2018.01.012>
31. Martin-Vide JP (2010) Local scour in a protruding wall on a river bank. *J Hydraul Res* 45(5):710–714
32. Martin-Vide JP, Roca M, Alvarado-Ancieta CA (2011) Bend scour protection using riprap. *Water Manag* 163(WM10):489–497
33. Maynard ST (1996) Toe scour estimation in stabilized bendways. *J Hydraul Eng* 122(8):460–464
34. Maynard ST (1997) Closure: toe-scour estimation in stabilized bendways. *J Hydraul Eng* 123(11):1048–1050
35. Molinas A, Kheireldin K, Wu B (1998) Local scour and flow measurement around bridge abutments. *J Hydraul Eng* 124:822–830. <https://doi.org/10.1080/00221689409498707>
36. Paola C, Voller VR (2005) A generalized exner equation for sediment mass balance. *J Geophys Res* 110:F04014
37. Rajaratnam BN, Nwachukwu BA (1983) Flow near groin-like structure. *J Hydraul Eng* 109:463–480
38. Sotiropoulos F, Diplas P (2017) Scour at the base of retaining walls and other longitudinal structures. Tech. Rep. 100, National Cooperative Highway Research Program, National Academies of Science, Washington, D.C.
39. Van Rijn LC (1993) Principles of sediment transport in rivers, estuaries, and coastal seas. Aqua Publications, Amsterdam
40. Wilcox DC (1994) Simulation of transition with two-equation turbulence model. *Am Inst Aeronaut Astronaut J* 42(2):247–255
41. Wu W, Rodi W, Wenka T (2000) 3d numerical modeling of flow and sediment transport in open channels. *J Hydraul Eng* 126(1):4–15
42. Zedler EA, Street RL (2001) Large-eddy simulation of sediment transport: currents over ripples. *J Hydraul Eng* 127(6):444–452

43. Zhang H, Nakagawa H, Kawaike K, Baba Y (2009) Experiment and simulation of turbulent flow in local scour around a spur dyke. *Int J Sediment Res* 24:33–45. [https://doi.org/10.1016/S1001-6279\(09\)60014-7](https://doi.org/10.1016/S1001-6279(09)60014-7)

Publisher's Note Springer Nature remains neutral with regard to jurisdictional claims in published maps and institutional affiliations.